Origin of Phase Transitions in Inorganic Lead Halide Perovskites: Interplay between Harmonic and Anharmonic Vibrations

Zhi-Gang Li, Marios Zacharias, Ying Zhang, Fengxia Wei, Yan Qin, Yong-Qing Yang, Lian-Cai An, Fei-Fei Gao, Wei Li, Jacky Even, et al.

Origin of phase transitions in inorganic lead halide perovskites: interplay between harmonic and anharmonic vibrations

Zhi-Gang Li[1], Marios Zacharias[2], Ying Zhang[1], Fengxia Wei[3], Yan Qin[1], Yong-Qing Yang[4], Lian-Cai An[1], Fei-Fei Gao[1], Wei Li,[1] Jacky Even,[2]* Xian-He Bu[1]**

1. School of Materials Science and Engineering, Smart Sensing Interdisciplinary Science Center, Nankai University & TKL of Metal and Molecule Based Material Chemistry, Tianjin 300350, China

2. Univ Rennes, INSA Rennes, CNRS, Institut FOTON, UMR 6082, Rennes F-35000, France

3. Institute of Materials Research and Engineering, Agency for Science, Technology and Research, Singapore 138634, Singapore

4. Department of Electrical and Computer Engineering, National University of Singapore, Singapore 117576, Singapore

ABSTRACT: Inorganic lead halide perovskites (ILHPs) exhibit a series of phase transitions and stabilization of the phases with desirable optoelectronic properties remains a major challenge. However, the intrinsic origins of structural instabilities in $CsPbX_3$ (X = Br, I) is still elusive. Herein, the important role of harmonic and anharmonic vibrations in influencing thermodynamic fluctuations of ILHPs was revealed, through combined lattice dynamics and multi-phonon theory calculations, and verified by diffraction experiments. Our results demonstrate that the transition between the δ- to γ-$CsPbI_3$ is driven by harmonic vibrations, unveiling the mysterious mechanism for stabilizing γ-$CsPbI_3$ via applying strain. Moreover, the successive transitions from the α- to β- and the β- to γ-phases of $CsPbX_3$ are driven by anharmonic vibrations. These structural dynamics are strongly coherent with the phonon diffuse scattering, substantially affecting the thermal conductivity and carrier relaxation. This work provides guidelines for maintaining favorable ILHP phases through delicately manipulating their lattice dynamics.

TOC GRAPHICS

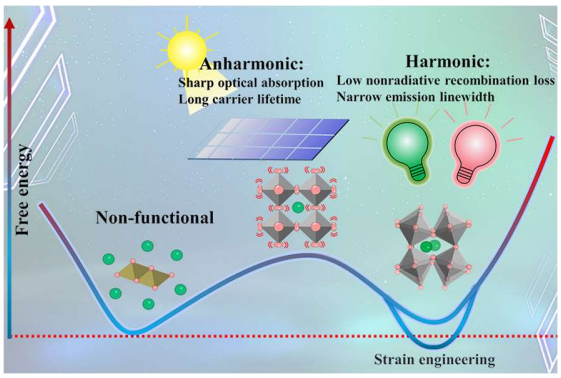

Inorganic lead halide perovskites (ILHPs) have been shown to exhibit outstanding optoelectronic and photovoltaic properties, superior stability compared with their hybrid counterparts[1-6]. $CsPbBr_3$ is a promising candidate for future optoelectronic devices because of its

tunable and narrow emission bandwidth, high defect tolerance, and striking photoluminescence quantum yield[7-10]. Meanwhile, solar cells based on the black metastable phase of $CsPbI_3$ have now surpassed 20% efficiencies due to its optimal bandgap, large charge carrier mobility, and lifetime product, etc. [11-13] However, these ILHPs exhibit lattice softness, making them vulnerable to a series of phase transitions upon thermodynamic perturbation, which often lead to significant changes in their intrinsic properties, generation of lattice strain, and hence largely impact their corresponding applications[14-19]. Moreover, the photovoltaic efficient γ-$CsPbI_3$ tends to transform into the non-functional δ-phase at ambient conditions, which is detrimental to the long-term reliability and durability [20-21].

To effectively stabilize the high-performance ILHPs phases, the atomistic origins of their structural instabilities need to be thoroughly elucidated. In terms of thermally driven phase transitions, lattice dynamics and structural fluctuations have been confirmed to play an important role [22-25]. Recent studies have shown that ILHPs exhibit significant anharmonic characteristics at high temperatures[17,19], which can strongly couple to charge carriers and influence some key optoelectronic properties such as carrier lifetime[26], excited-state dynamics[27-30], electronic bandgap[15], joint density of states (JDOS)[31], trap states[32], the Urbach energy[33], ion diffusion and carrier recombination[34-35], whereas the relationship between anharmonicity and phase transitions remains unclear. Here, we study the origin of phase transitions in $CsPbBr_3$ and $CsPbI_3$ (Figures 1a-d), disclosing that the interplay between harmonic and anharmonic vibrations plays a crucial role in determining their phase stabilities.

Reconstructive phase transition induced by harmonic fluctuation

Lattice dynamics calculations were performed to investigate the effect of atomic vibrations on the phase transition between the δ- and metastable γ-$CsPbI_3$. There are no imaginary frequency

modes from the calculated phonon spectra of both phases, indicating that both polymorphs are dynamically stable (Figure S4). This result is consistent with previous *ab* initio calculations[36]. Moreover, the calculated elastic constants show that both phases are stable according to the elastic stability criteria of the orthorhombic system (Table S1). In this regard, the thermodynamic instability is neither caused by critical fluctuations related to a displacive soft optical phonon, thus confirming the reconstructive and first order character of the γ- to δ-$CsPbI_3$ phase transition.

Taking only the contribution of vibrational entropy into consideration, the Gibbs free energy can be expressed as: $G \approx U + F_{vib} = U_0 + E_{vib} - TS_{vib}$. Here, U, F_{vib}, U_0, E_{vib} and S_{vib} are the total internal energy, phonon free energy, the internal energy at 0 K, the vibrational energy and the vibrational entropy, respectively. The E_{vib} and S_{vib} are temperature-dependent, given by:

$$E_{vib} = \int_0^\infty g(\varepsilon)\, \varepsilon[n(\varepsilon,T) + 1/2]d\varepsilon \quad (1)$$

$$S_{vib}(T) = 3k_B \int_0^\infty g(\varepsilon)\{[n(\varepsilon,T)+1]ln[n(\varepsilon,T)+1] - n(\varepsilon)ln[n(\varepsilon,T)]\}d\varepsilon \quad (2)$$

where ω is the phonon mode frequency, k_B is the Boltzmann constant, g(ε) is the normalized phonon DOS with energy $\varepsilon = \hbar\omega$, $n(\varepsilon,T)$ is the Bose-Einstein population of a state of energy ε at temperature T. Let us note here that the temperature dependence of S_{vib} comes entirely from the Bose-Einstein phonon population, assuming that the variation of the phonon dispersion at finite temperatures remains nearly constant[37]. As seen in Figure 1e, the S_{vib} of γ-$CsPbI_3$ is always higher than that of δ-$CsPbI_3$, and the difference of their vibrational entropy ΔS_{vib} remains constant around 14 J $K^{-1}mol^{-1}$ in the high-temperature regime. The δ-phase is therefore predicted to become metastable since the energy affected by ΔS_{vib} offsets the difference of the internal energy ΔU at about 340 K, hence manifesting its vibrational entropy-driven nature for the phase transition.

The concept of size mismatch can be used to explain the origin of the difference in S_{vib}[38], when softer or stiffer local structures are caused by the change of coordination environment of atoms with different sizes, leading to a difference in vibrational energies between two phases. The γ- to δ-$CsPbI_3$ transition involves a dramatic change in the packing density and rearrangement of the atomic coordination environments (Figures 1c-d), and the δ-$CsPbI_3$ owns a relatively small unit cell with octahedra packed more tightly along the direction of $[PbI_6]^{4-}$ double chains. Thus, the amplitudes of atomic vibrations in this direction are significantly reduced and the structure of δ-$CsPbI_3$ tends to be locally stiffer.

To further analyze the vibrational effects between these two phases, the difference of phonon density of states (DOS) (ΔDOS = DOS_δ - DOS_γ) are shown in Figure 1f, which reveals that ΔDOS at low frequencies (below 1 THz) caused by the motions of I and Cs atoms, are responsible for the large ΔS_{vib}. Notably, the increased phonon DOS of δ-$CsPbI_3$ at high-frequency modes indicates its stiffer nature compared with γ-$CsPbI_3$. The strongest effects occur at the *S* (-0.5 0.5 0.0) π/a and *Y* (0.0 0.5 0.0) π/a points in the Brillouin zone, corresponding to the direction of PbI_6 octahedra double chains. These edge-sharing octahedra in the δ-phase are more tightly packed than the corner-sharing octahedra in the γ-phase, resulting in harder shear phonon modes in the former (Figures S1 and S2). These results clearly indicate that the difference in stacked configurations of PbI_6 octahedra is the main source of the ΔS_{vib} between the γ- and δ-phases.

Based on the analyses above, tuning ΔS_{vib} between the γ- and δ-phase could be an effective way to suppress the phase transition and stabilize γ-phase at room temperature (Figure S5). Accordingly, a set of uniaxially strained γ-$CsPbI_3$ structures were calculated (see the Method section for details), and the results show that the $CsPbI_3$ structure is dynamically stable if the applied strain along [001] direction is less than 2%. However, when the applied strain reaches

2.5%, imaginary phonon modes arise, showing a characteristic dynamic instability (Figure S6). With increasing strain, the phonon energy of γ-$CsPbI_3$ gradually decreases, which, in turn, gives rise to a monotonically increased S_{vib} (Figure 2a-b). In addition, the phase transition temperatures under different strains were calculated, and the results indicate that the increase of strain enlarges ΔS_{vib}, hence decreasing the temperature at which the δ-$CsPbI_3$ becomes metastable (Figure 2c). With the strain increasing from 0 to 2%, this temperature decreases from 340 to 220 K, showing that photovoltaic γ-$CsPbI_3$ could be made thermodynamically stable at room temperature by applying external stress. Furthermore, the bandgap of γ-$CsPbI_3$ varies rather little under different strain conditions (Figure S7), indicating that mild uniaxial strain would not affect its photovoltaic performance.

Order-disorder phase transition induced by lattice anharmonicity

Our analysis indicates that the structural phase transitions between β- and γ-$CsPbX_3$ exhibit weak anharmonic features (Figure S8-S12, Table S2). Furthermore, the β- to α- phase transition, occurs at about 403 and 533 K for $CsPbBr_3$ and $CsPbI_3$, respectively (Figure S3), showing a first-order characteristic. This observation is consistent with a previous one on $CsPbCl_3$. However as explained in the supporting information, such a first order transition can be classified as weakly first order according to its order parameter free energy expansion within Landau theory, by opposition to the reconstructive and (strongly) first order character of the γ- to δ-$CsPbI_3$ phase transition. This analysis is proposed by considering the low and high temperature space groups for the β- to α- and γ- to δ-$CsPbI_3$ phase transitions. The phonon spectra and DOSs of the α-phase $CsPbX_3$ (Figure S13 and S14) show that additional imaginary phonon modes, ranging from -0.5 to -1 THz, are present compared with the β-phase, which are mainly driven by the motions of halide X atoms. The phonon band structures display soft phonon modes distributed throughout the

Brillouin zone, where the maxima of negative frequencies are located at both the *M* (0,0.5,0.5) π/a and *R* (0.5,0.5,0.5) π/a points. Combining the normal modes at the *M* and *R* points, the potential energy surface of α-$CsPbBr_3$ (Figure 3c) was calculated to show four potential wells, which can be divided into two groups. Let us note that because the β-phase belongs to the *P*4/*mbm* space group, only the operation of M_3^+ can lead to the correct atomic coordinates, and the motions of halide X atoms corresponding to phonon mode mentioned above are shown in Figure 3d.

However, the group theory analysis does not give an indication about the PL evolution in such highly anharmonic systems. As seen in Figure 4a, the PL peaks exhibit a continuous blue shift when $CsPbBr_3$ transforms from the β- to α-phase, which is contrary to the case of the γ- *to* β-phase transition (Supporting Information). As mentioned above, it corresponds to the expected effect related mostly to a volumetric expansion of the lattice. Moreover, $CsPbBr_3$ does not have an ideal cubic symmetry but is dynamically/statically disordered in the high-temperature α-phase[39-40]. Thus, a major impediment to truly elucidate the origin of β- to α-phase transition come to the confirmation that octahedral rotations are truly static or rather dynamically fluctuating. The two-dimensional (2D) probability distribution function (PDF) was utilized to quantify the dynamic atomic positions. The PDF data (Figure 3b) obtained from the AIMD calculations shows that Br atoms are distributed in a spherical shape perpendicular to the Pb-Br-Pb direction (in-plane) but a rod-shaped along the Pb-Br-Pb bond direction (out-of-plane), which are well consistent with the measured structural anisotropy from single-crystal X-ray diffraction (SCXRD). It can be concluded that the Br atoms present obvious anisotropic vibrations: strong in-plane but weak out-of-plane vibrations. In addition, both the calculated and experimentally determined atomic displacements (Figure 3a) show large displacement of in-plane Br atoms, which further reveal that disorder in the α-phase is derived to a large extent from the dynamic fluctuations of Br atoms.

However quasistatic or ultraslow motions not captured within the time-window of AIMD may also exist as shown by experimental techniques such as high-resolution inelastic neutron scattering or Brillouin scattering down to the sub-GHz range in iodide and bromide hybrid 3D perovskites[41].

Variable-temperature SCXRD experiments were performed to further clarify the role of dynamic fluctuations of Br atoms in this phase transition. The lattice constant, *c*, extracted from SCXRD (Figure S15), contracts upon heating in the range of the β phase. Since the *c*-axis corresponds to the direction along the Pb-Br-Pb bond, its negative thermal expansion (NTE) would be caused by the rocking motions of the Br atoms in the direction perpendicular to the Pb-Br-Pb orientation[42]. This is further supported by the sudden increase of the transverse atomic displacement parameter U_{33} of the Br atom (Figure 4d).

The probabilities of the Br atoms rocking in all directions perpendicular to the *c*-axis are similar so the average positions are still in the middle of the two adjacent Pb atoms, therefore the dynamic disorder would not be observed at high temperatures. Raman spectra reveal two distinct peaks at about 44 and 67 cm^{-1}, the former is assigned to head-to-head Cs motion and Pb-Br stretch while the latter is dominated by the motions of Br perpendicular to Pb-Br-Pb bond [43]. The unusual stiffening of the low-frequency peak is observed upon heating from 383 to 423 K, indicating that the force constant of Pb-Br bond-stretching increases continuously with rising temperature, which is consistent with the NTE behavior of the *c*-axis mentioned above. Furthermore, it is energetically favorable due to the fact that the softening of the high-frequency peak increases the vibration entropy during phase transition, suggesting that the strong rocking motions of Br are responsible for the β- to α-phase transition of $CsPbBr_3$.

The potential well model theoretically elucidates the reason regarding the large fluctuation of Br atoms. The potential well depth of $CsPbX_3$ (Figure S16) at the *M* point (48.89 meV for $CsPbBr_3$

and 66.83 meV for $CsPbI_3$) is about 1.5 times of K_BT (34.88 meV for $CsPbBr_3$ and 46.13 meV for $CsPbI_3$), indicating the energy provided by the harmonic interactions between nearest-neighboring atoms are significantly weakened to result in short-range disorder. In other words, the β- to α-phase transition is driven by the strong anharmonic disorder motions of halide atoms. Moreover, the AIMD results (Figure S13) show these α-$CsPbX_3$ would be dynamically stable at high temperatures after taking into account the anharmonic vibrations. As $CsPbX_3$ does not present a static cubic structure at high temperature, an increase in bandgap on heating appears.

Anharmonic lattice dynamics and phonon diffuse scattering

Due to the intricate nature of the anharmonic effects in these compounds, that is related to electron and lattice heat transfer, the process of elucidating such mechanisms involves the consideration of multiple phonons, such as the non-standard temperature dependence of thermal conductivities as well as thermal carrier and phonon relaxation[44]. One of the main challenges arising from such approach is to clearly distinguish the role of multiple phonons from individual ones in anharmonic processes to facilitate a comprehensive understanding of the phonons scattering behaviors. Multi-phonon scattering refers to a process in which more than one phonon is created or annihilated during inelastic scattering experiments (Figures 5 (a) and (b)). This process generally occurs in high order Brillouin zone and under high temperature conditions. Typical contributions to inelastic scattering signals arising from multi-phonon processes usually involve the low-frequency acoustic modes which exhibit a high-degree of anharmonicity [45]. To further comprehend and analyze the scattering signatures of individual phonons in ILHPs, thermal diffuse scattering calculations were performed based on the Laval-Born-James (LBJ) theory to probe multi-phonon contributions across several Brillouin zones in the reciprocal space [46]. The all-phonon LBJ scattering intensity can be calculated from the following expression:

$$I_{all}(Q,T) = N_p \sum_{p} \sum_{kk\prime} f_k(Q) f_{k\prime}(Q) e^{iQ\cdot[R_p+\tau_k-\tau_{k\prime}]} \times e^{-W_k(Q,T)} e^{-W_{k\prime}(Q,T)} e^{P_{p,kk}(Q,T)} \quad (3)$$

Where N_p is the number of **q**-points used to sample the first Brillouin Zone, τ_k represents the atomic positions, and R_p defines the position vectors of unit cell p contained in a periodic supercell, $f_\kappa(Q)$ denotes the scattering amplitude of atom κ, and $W_k(Q,T)$ is the Debye-Waller factor. The phononic factor, $P_{p,kk\prime}(Q,T)$, can be obtained as follows:

$$P_{p,kk\prime}(Q,T) = \frac{M_0 N_p^{-1}}{\sqrt{M_k M_{k\prime}}} \sum_{qv} u_{qv}^2 \Re\left[Q \cdot e_{k,v}(q) Q \cdot e_{k\prime,v}(q) e^{iq\cdot R_p}\right] \quad (4)$$

where M_κ and M_0 are the atomic and reference masses, and v denotes the phonon branch index. The mode-resolved mean-square displacements of the atoms are defined as $u_{qv}^2 = \hbar/\left(2M_0 w_{qv}\right)\left[2n_{qv}(T)+1\right]$, where $n_{qv}(T)$ is the Bose-Einstein distribution. Following the derivation in Ref. [45] applying the Taylor expansion to the phononic factor $P_{p,kk\prime}(Q,T)$ in Equation (4), and keeping only the zeroth-order term yields the Bragg diffraction intensity as follows:

$$I_0(Q,T) = N_p^2 \sum_{kk\prime} f_k(Q) f_{k\prime}(Q) cos[Q\cdot(\tau_k - \tau_{k\prime})] \times e^{-W_k(Q,T)} e^{-W_{k\prime}(Q,T)} \delta_{Q,G}, \quad (5)$$

where we have employed the sum rule $\sum pexp\left(iQ\cdot R_p\right) = N_p \delta_{Q,G}$. In the same spirit, the one-phonon scattering formula can be expressed as [45]:

$$I_1(Q,T) = M_0 N_p \sum_{kk\prime} f_k(Q) f_{k\prime}(Q) \frac{e^{-W_k(Q,T)} e^{-W_{k\prime}(Q,T)}}{\sqrt{M_k M_{k\prime}}} \times \sum_{v} \Re\left[Q\cdot e_{k,v}(Q) Q \cdot e_{k\prime,v}(Q) e^{iQ\cdot[\tau_{k\prime}-\tau_k]}\right] u^2{}_{Qv} \quad (6)$$

Thus, the multi-phonon scattering can be written as:

$$I_{multi}(Q,T) = I_{all}(Q,T) - I_0(Q,T) - I_1(Q,T) \quad (7)$$

Figures 5 (c-f) show the all-phonon diffuse scattering intensity and percentage contribution of multi-phonon scattering *P* of $CsPbBr_3$ and $CsPbI_3$, calculated using the ZG module of EPW [please cite arxiv:2302.08085, if you have no space add this in the caption of Figure 5]. Our results reveal a high degree of anisotropy in thermal phonon populations. The red features in Figure 5 (c) and (e) indicate the enhancement in diffuse scattering intensity around the M point in momentum space, corresponding to cooperative rotations of PbX_6 octahedra with limited Cs atom involvement. However, no significant scattering characteristic have been observed along the G-X direction. This structural dynamics of cubic LHPs strongly overlap with the distortions at the phase transitions. It is worth mentioning that there are analogous contributory effects of multi-phonon processes in both compounds, which is even comparable to one-phonon scattering intensity at Q_x = 6 $Å^{-1}$ for $CsPbBr_3$ and $CsPbI_3$ around the M point (Figures 5 (c) and (d)). These acoustic soft modes will drive anharmonicity at high temperatures and also be responsible for the largest contribution to multi-phonon interactions. Multi-phonon diffuse scattering calculations can potentially yield unexplored details of non-equilibrium phonon populations in LHPs and indicate that anharmonic fluctuations associated with transversal motions of halide atoms can become more pronounced with increasing temperature (Figure S17).

In summary, our lattice dynamic calculations have shown that both the γ- and δ-$CsPbI_3$ present harmonic energy landscape around equilibrium, and the phase transition arises from the significant entropy change between the two phases due to the difference of harmonic lattice vibrational frequencies. Uniaxial strain applied in γ-$CsPbI_3$ can further enlarge the vibrational entropy change and decrease the phase transition temperature, enabling the preservation of the metastable but technologically important γ-$CsPbI_3$ at room temperature. Moreover, the γ- to β- phase transitions

of $CsPbX_3$ exhibit a second-order characteristic with the rotation angles of the PbX_6 octahedra as the primary order parameter, which leads to abnormal changes in the electronic structures and lattice stiffness. Furthermore, we unravel that the transverse motions of halogen atoms, which present strong anharmonic features, are accountable for the β- to α- transitions of $CsPbX_3$. Such anharmonic vibrations induced phases are imperfect cubic structures characteristic of octahedral tilting with a disordered manner. This work reveals the atomistic and electronic origins of phase transitions in ILHPs, which not only provides thermodynamic insights for obtaining technologically important phases but also offers possibilities for improving their optoelectronic properties by leveraging the harmonicity and anharmonicity of their lattice dynamics.

ASSOCIATED CONTENT

Supporting Information.

The Supporting Information is available free of charge at: https://pubs.acs.org/doi...

Additional experimental details, materials and computational methods, mechanical properties and elastic constants of γ-$CsPbI_3$ and δ-$CsPbI_3$, structural phase transitions between β- and γ-$CsPbX_3$, electronic structures of γ-$CsPbBr_3$ and β-$CsPbBr_3$, phonon dispersion relations and DOSs, temperature dependence of the lattice parameters of $CsPbBr_3$.

AUTHOR INFORMATION

Corresponding Authors

Wei Li — School of Materials Science and Engineering & Tianjin Key Laboratory of Metal and Molecule-Based Material Chemistry, Nankai University, Tianjin 300350, China; Email: wl276@nankai.edu.cn

Jacky Even — Univ Rennes, INSA Rennes, CNRS, Institut FOTON, UMR 6082, Rennes F-35000, France; Email: Jacky.Even@insa-rennes.fr

Xian-He Bu — School of Materials Science and Engineering & Tianjin Key Laboratory of Metal and Molecule-Based Material Chemistry, Nankai University, Tianjin 300350, China; Email: buxh@nankai.edu.cn

Authors

Zhi-Gang Li—School of Materials Science and Engineering & Tianjin Key Laboratory of Metal and Molecule-Based Material Chemistry, Nankai University, Tianjin 300350, China

Marios Zacharias—Univ Rennes, INSA Rennes, CNRS, Institut FOTON, UMR 6082, Rennes F-35000, France

Ying Zhang—School of Materials Science and Engineering & Tianjin Key Laboratory of Metal and Molecule-Based Material Chemistry, Nankai University, Tianjin 300350, China

Fengxia Wei— Institute of Materials Research and Engineering, Agency for Science, Technology and Research, Singapore 138634, Singapore

Yan Qin—School of Materials Science and Engineering & Tianjin Key Laboratory of Metal and Molecule-Based Material Chemistry, Nankai University, Tianjin 300350, China

Yong-Qing Yang—Department of Electrical and Computer Engineering, National University of Singapore, Singapore 117576, Singapore

Lian-Cai An—School of Materials Science and Engineering & Tianjin Key Laboratory of Metal and Molecule-Based Material Chemistry, Nankai University, Tianjin 300350, China

Fei-Fei Gao—School of Materials Science and Engineering & Tianjin Key Laboratory of Metal and Molecule-Based Material Chemistry, Nankai University, Tianjin 300350, China

Author Contributions

Z.-G.L., W.L. and X.-H.B. designed and organized the research. Z.-G.L. and Y. Z. prepared single crystals. Z.-G.L. and L.-C.A. performed VT single crystal X-ray measurements. Z.-G.L. and Y.Q. performed VT-PL measurements. Z.-G.L. and F.-F.G. performed VT-Raman measurements. Z.-G.L. performed the theoretical calculations under the guidance of M.Z., W.L. and J.E. Data analysis was performed by Z.-G.L., M.Z., Y.Q., Y.Q.Y., J.E. and W.L. Z.-G.L. wrote the full manuscript, F.W.,W.L., J.E. and X.-H.B. revised the manuscript.

Notes

The authors declare no competing financial interest.

ACKNOWLEDGMENT

We acknowledge the financial support from the National Natural Science Foundation of China (Nos.21975132 and 21991143) and the Fundamental Research Funds for the Central Universities (No.63196006). M.Z. was funded by the European Union (project ULTRA-2DPK / HORIZON-MSCA-2022-PF-01 / Grant Agreement No. 101106654). Views and opinions expressed are however those of the authors only and do not necessarily reflect those of the European Union or the European Commission. Neither the European Union nor the granting authority can be held responsible for them.

REFERENCES

(1) Chen, Q.; Wu, J.; Ou, X.; Huang, B.; Almutlaq, J.; Zhumekenov, A. A.; Guan, X.; Han, S.; Liang, L.; Yi, Z.; Li, J.; Xie, X.; Wang, Y.; Li, Y.; Fan, D.; Teh, D. B. L.; All, A. H.; Mohammed, O. F.; Bakr, O. M.; Wu, T.; Bettinelli, M.; Yang, H.; Huang, W.; Liu, X. All-inorganic perovskite nanocrystal scintillators. *Nature* **2018,** *561* (7721), 88—93.

(2) Kovalenko, M. V.; Protesescu, L.; Bodnarchuk, M. I. Properties and potential optoelectronic applications of lead halide perovskite nanocrystals. *Science* **2017,** *358* (6364), 745—750.

(3) Koscher, B. A.; Swabeck, J. K.; Bronstein, N. D.; Alivisatos, A. P. Essentially trap-free $CsPbBr_3$ colloidal nanocrystals by postsynthetic thiocyanate surface treatment. *J. Am. Chem. Soc.* **2017,** *139* (19), 6566—6569.

(4) Swarnkar, A.; Marshall, A. R.; Sanehira, E. M.; Chernomordik, B. D.; Moore, D. T.; Christians, J. A.; Chakrabarti, T.; Luther, J. M. Quantum dot–induced phase stabilization of α-$CsPbI_3$ perovskite for high-efficiency photovoltaics. *Science* **2016,** *354* (6308), 92—95.

(5) Hou, J.; Chen, P.; Shukla, A.; Krajnc, A.; Wang, T.; Li, X.; Doasa, R.; Tizei, L. H. G.; Chan, B.; Johnstone, D. N.; Lin, R.; Schülli, T. U.; Martens, I.; Appadoo, D.; Ari, M. S.; Wang, Z.; Wei, T.; Lo, S.-C.; Lu, M.; Li, S.; Namdas, E. B.; Mali, G.; Cheetham, A. K.; Collins, S. M.; Chen, V.; Wang, L.; Bennett, T. D. Liquid-phase sintering of lead halide perovskites and metal-organic framework glasses. *Science* **2021,** *374* (6567), 621—625.

(6) Fu, Y.; Zhu, H.; Stoumpos, C. C.; Ding, Q.; Wang, J.; Kanatzidis, M. G.; Zhu, X.; Jin, S. Broad wavelength tunable robust lasing from single-crystal nanowires of cesium lead halide perovskites ($CsPbX_3$, X = Cl, Br, I). *ACS Nano* **2016,** *10* (8), 7963—7972.

(7) Swarnkar, A.; Chulliyil, R.; Ravi, V. K.; Irfanullah, M.; Chowdhury, A.; Nag, A. Colloidal $CsPbBr_3$ perovskite nanocrystals: Luminescence beyond traditional quantum dots. *Angew. Chem. Int. Ed.* **2015,** *54* (51), 15424—15428.

(8) Ling, Y.; Tian, Y.; Wang, X.; Wang, J. C.; Knox, J. M.; Perez-Orive, F.; Du, Y.; Tan, L.; Hanson, K.; Ma, B.; Gao, H. Enhanced optical and electrical properties of polymer-assisted all-inorganic perovskites for light-emitting diodes. *Adv. Mater.* **2016,** *28* (40), 8983—8989.

(9) Hu, X.; Zhou, H.; Jiang, Z.; Wang, X.; Yuan, S.; Lan, J.; Fu, Y.; Zhang, X.; Zheng, W.; Wang, X.; Zhu, X.; Liao, L.; Xu, G.; Jin, S.; Pan, A. Direct vapor growth of perovskite $CsPbBr_3$ nanoplate electroluminescence devices. *ACS Nano* **2017,** *11* (10), 9869—9876.

(10) Shi, Z.; Li, Y.; Zhang, Y.; Chen, Y.; Li, X.; Wu, D.; Xu, T.; Shan, C.; Du, G. High-efficiency and air-stable perovskite quantum dots light-emitting diodes with an all-inorganic heterostructure. *Nano Lett.* **2017,** *17* (1), 313—321.

(11) Yoon, S. M.; Min, H.; Kim, J. B.; Kim, G.; Lee, K. S.; Seok, S. I. Surface engineering of ambient-air-processed cesium lead triiodide layers for efficient solar cells. *Joule* **2021,** *5* (1), 183—196.

(12) Xiang, W.; Liu, S.; Tress, W. A review on the stability of inorganic metal halide perovskites: Challenges and opportunities for stable solar cells. *Energy Environ. Sci.* **2021,** *14* (4), 2090—2113.

(13) Wang, Y.; Dar, M. I.; Ono, L. K.; Zhang, T.; Kan, M.; Li, Y.; Zhang, L.; Wang, X.; Yang, Y.; Gao, X.; Qi, Y.; Grätzel, M.; Zhao, Y. Thermodynamically stabilized β-$CsPbI_3$–based perovskite solar cells with efficiencies >18%. *Science* **2019,** *365* (6453), 591—595.

(14) Lin, J.; Lai, M.; Dou, L.; Kley, C. S.; Chen, H.; Peng, F.; Sun, J.; Lu, D.; Hawks, S. A.; Xie, C.; Cui, F.; Alivisatos, A. P.; Limmer, D. T.; Yang, P. Thermochromic halide perovskite solar cells. *Nat. Mater.* **2018,** *17* (3), 261—267.

(15) Lanigan-Atkins, T.; He, X.; Krogstad, M. J.; Pajerowski, D. M.; Abernathy, D. L.; Xu, G. N. M. N.; Xu, Z.; Chung, D. Y.; Kanatzidis, M. G.; Rosenkranz, S.; Osborn, R.; Delaire, O. Two-dimensional overdamped fluctuations of the soft perovskite lattice in $CsPbBr_3$. *Nat. Mater.* **2021,** *20* (7), 977—983.

(16) Sutton, R. J.; Filip, M. R.; Haghighirad, A. A.; Sakai, N.; Wenger, B.; Giustino, F.; Snaith, H. J. Cubic or orthorhombic? Revealing the crystal structure of metastable black-phase $CsPbI_3$ by theory and experiment. *ACS Energy Lett.* **2018,** *3* (8), 1787—1794.

(17) Marronnier, A.; Roma, G.; Boyer-Richard, S.; Pedesseau, L.; Jancu, J.-M.; Bonnassieux, Y.; Katan, C.; Stoumpos, C. C.; Kanatzidis, M. G.; Even, J. Anharmonicity and disorder in the black phases of cesium lead iodide used for stable inorganic perovskite solar cells. *ACS Nano* **2018,** *12* (4), 3477—3486.

(18) Straus, D. B.; Guo, S.; Cava, R. J. Kinetically stable single crystals of perovskite-phase $CsPbI_3$. *J. Am. Chem. Soc.* **2019,** *141* (29), 11435—11439.

(19) Marronnier, A.; Lee, H.; Geffroy, B.; Even, J.; Bonnassieux, Y.; Roma, G. Structural instabilities related to highly anharmonic phonons in halide perovskites. *J. Phys. Chem. Lett.* **2017,** *8* (12), 2659—2665.

(20) Steele, J. A.; Jin, H.; Dovgaliuk, I.; Berger, R. F.; Braeckevelt, T.; Yuan, H.; Martin, C.; Solano, E.; Lejaeghere, K.; Rogge, S. M. J.; Notebaert, C.; Vandezande, W.; Janssen, K. P. F.;

Goderis, B.; Debroye, E.; Wang, Y.-K.; Dong, Y.; Ma, D.; Saidaminov, M.; Tan, H.; Lu, Z.; Dyadkin, V.; Chernyshov, D.; Van Speybroeck, V.; Sargent, E. H.; Hofkens, J.; Roeffaers, M. B. J. Thermal unequilibrium of strained black $CsPbI_3$ thin films. *Science* **2019,** *365* (6454), 679—684.

(21) Ke, F.; Wang, C.; Jia, C.; Wolf, N. R.; Yan, J.; Niu, S.; Devereaux, T. P.; Karunadasa, H. I.; Mao, W. L.; Lin, Y. Preserving a robust $CsPbI_3$ perovskite phase via pressure-directed octahedral tilt. *Nat. Commun.* **2021,** *12* (1), 461.

(22) Dove, M. T. Theory of displacive phase transitions in minerals. *Am. Mineral.* **1997,** *82* (3-4), 213—244.

(23) Budai, J. D.; Hong, J.; Manley, M. E.; Specht, E. D.; Li, C. W.; Tischler, J. Z.; Abernathy, D. L.; Said, A. H.; Leu, B. M.; Boatner, L. A.; McQueeney, R. J.; Delaire, O. Metallization of vanadium dioxide driven by large phonon entropy. *Nature* **2014,** *515* (7528), 535—539.

(24) Wei, W.; Li, W.; Butler, K. T.; Feng, G.; Howard, C. J.; Carpenter, M. A.; Lu, P.; Walsh, A.; Cheetham, A. K. An unusual phase transition driven by vibrational entropy changes in a hybrid organic–inorganic perovskite. *Angew. Chem. Int. Ed.* **2018,** *57* (29), 8932—8936.

(25) Li, K.; Li, Z.-G.; Xu, J.; Qin, Y.; Li, W.; Stroppa, A.; Butler, K. T.; Howard, C. J.; Dove, M. T.; Cheetham, A. K.; Bu, X.-H. Origin of ferroelectricity in two prototypical hybrid organic–inorganic perovskites. *J. Am. Chem. Soc.* **2022,** *144* (2), 816—823.

(26) Li, W.; Vasenko, A. S.; Tang, J.; Prezhdo, O. V. Anharmonicity extends carrier lifetimes in lead halide perovskites at elevated temperatures. *J. Phys. Chem. Lett.* **2019,** *10* (20), 6219—6226.

(27) Shi, R.; Fang, Q.; Vasenko, A. S.; Long, R.; Fang, W.-H.; Prezhdo, O. V., Structural disorder in higher-temperature phases increases charge carrier lifetimes in metal halide perovskites. *J. Am. Chem. Soc.* **2022,** *144* (41), 19137—19149.

(28) Wang, Y.; Long, R., Anomalous temperature-dependent charge recombination in $CH_3NH_3PbI_3$ perovskite: key roles of charge localization and thermal effect. *ACS Appl. Mater. Interfaces* **2019,** *11* (35), 32069—32075.

(29) Lu, H.; Fang, W.-H.; Long, R., Collective motion improves the stability and charge carrier lifetime of metal halide perovskites: a phonon-resolved nonadiabatic molecular dynamics study. *J. Phys. Chem. Lett.* **2022,** *13* (13), 3016—3022.

(30) Liu, Y.; Long, R.; Fang, W.-H., Great influence of organic cation motion on charge carrier dynamics in metal halide perovskite unraveled by unsupervised machine learning. *J. Phys. Chem. Lett.* **2022,** *13* (36), 8537—8545.

(31) Gehrmann, C.; Caicedo-Dávila, S.; Zhu, X.; Egger, D. A. Transversal halide motion intensifies band-to-band transitions in halide perovskites. *Adv. Sci.* **2022,** *9* (16), 2200706.

(32) Chu, W.; Saidi, W. A.; Zhao, J.; Prezhdo, O. V. Soft lattice and defect covalency rationalize tolerance of β-$CsPbI_3$ perovskite solar cells to native defects. *Angew. Chem. Int. Ed.* **2020,** *59* (16), 6435—6441.

(33) Gehrmann, C.; Egger, D. A. Dynamic shortening of disorder potentials in anharmonic halide perovskites. *Nat. Commun.* **2019,** *10* (1), 3141.

(34) Bischak, C. G.; Hetherington, C. L.; Wu, H.; Aloni, S.; Ogletree, D. F.; Limmer, D. T.; Ginsberg, N. S. Origin of reversible photoinduced phase separation in hybrid perovskites. *Nano Lett.* **2017,** *17* (2), 1028—1033.

(35) Munson, K. T.; Kennehan, E. R.; Doucette, G. S.; Asbury, J. B. Dynamic disorder dominates delocalization, transport, and recombination in halide perovskites. *Chem* **2018,** *4* (12), 2826—2843.

(36) Kaczkowski, J.; Płowaś-Korus, I. The vibrational and thermodynamic properties of $CsPbI_3$ polymorphs: An improved description based on the scan meta-GGA functional. *J. Phys. Chem. Lett.* **2021,** *12* (28), 6613—6621.

(37) Zhao, Y.; Zeng, S.; Li, G.; Lian, C.; Dai, Z.; Meng, S.; Ni, J. Lattice thermal conductivity including phonon frequency shifts and scattering rates induced by quartic anharmonicity in cubic oxide and fluoride perovskites. *Phys. Rev. B* **2021,** *104* (22), 224304.

(38) van de Walle, A.; Ceder, G. The effect of lattice vibrations on substitutional alloy thermodynamics. *Rev. Mod. Phys.* **2002,** *74* (1), 11—45.

(39) Zhao, X.-G.; Dalpian, G. M.; Wang, Z.; Zunger, A. Polymorphous nature of cubic halide perovskites. *Phys. Rev. B* **2020,** *101* (15), 155137.

(40) Zhao, X.-G.; Wang, Z.; Malyi, O. I.; Zunger, A. Effect of static local distortions vs. Dynamic motions on the stability and band gaps of cubic oxide and halide perovskites. *Mater. Today* **2021,** *49*, 107—122.

(41) Hehlen, B.; Bourges, P.; Rufflé, B.; Clément, S.; Vialla, R.; Ferreira, A. C.; Ecolivet, C.; Paofai, S.; Cordier, S.; Katan, C.; Létoublon, A.; Even, J. Pseudospin-phonon pretransitional dynamics in lead halide hybrid perovskites. *Phys. Rev. B* **2022,** *105* (2), 024306.

(42) Hu, L.; Chen, J.; Sanson, A.; Wu, H.; Guglieri Rodriguez, C.; Olivi, L.; Ren, Y.; Fan, L.; Deng, J.; Xing, X. New insights into the negative thermal expansion: Direct experimental evidence for the "guitar-string" effect in cubic ScF_3. *J. Am. Chem. Soc.* **2016,** *138* (27), 8320—8323.

(43) Yaffe, O.; Guo, Y.; Tan, L. Z.; Egger, D. A.; Hull, T.; Stoumpos, C. C.; Zheng, F.; Heinz, T. F.; Kronik, L.; Kanatzidis, M. G.; Owen, J. S.; Rappe, A. M.; Pimenta, M. A.; Brus, L. E. Local polar fluctuations in lead halide perovskite crystals. *Phys. Rev. Lett.* **2017,** *118* (13), 136001.

(44) Wu, T.; Chen, X.; Xie, H.; Chen, Z.; Zhang, L.; Pan, Z.; Zhuang, W., Coupling of spin-orbit interaction with phonon anharmonicity leads to significant impact on thermoelectricity in SnSe. *Nano Energy* **2019,** *60*, 673—679.

(45) Zacharias, M.; Seiler, H.; Caruso, F.; Zahn, D.; Giustino, F.; Kelires, P. C.; Ernstorfer, R. Multiphonon diffuse scattering in solids from first principles: Application to layered crystals and two-dimensional materials. *Phys. Rev. B* **2021,** *104* (20), 205109.

(46) Zacharias, M.; Seiler, H.; Caruso, F.; Zahn, D.; Giustino, F.; Kelires, P. C.; Ernstorfer, R. Efficient first-principles methodology for the calculation of the all-phonon inelastic scattering in solids. *Phys. Rev. Lett.* **2021,** *127* (20), 207401.

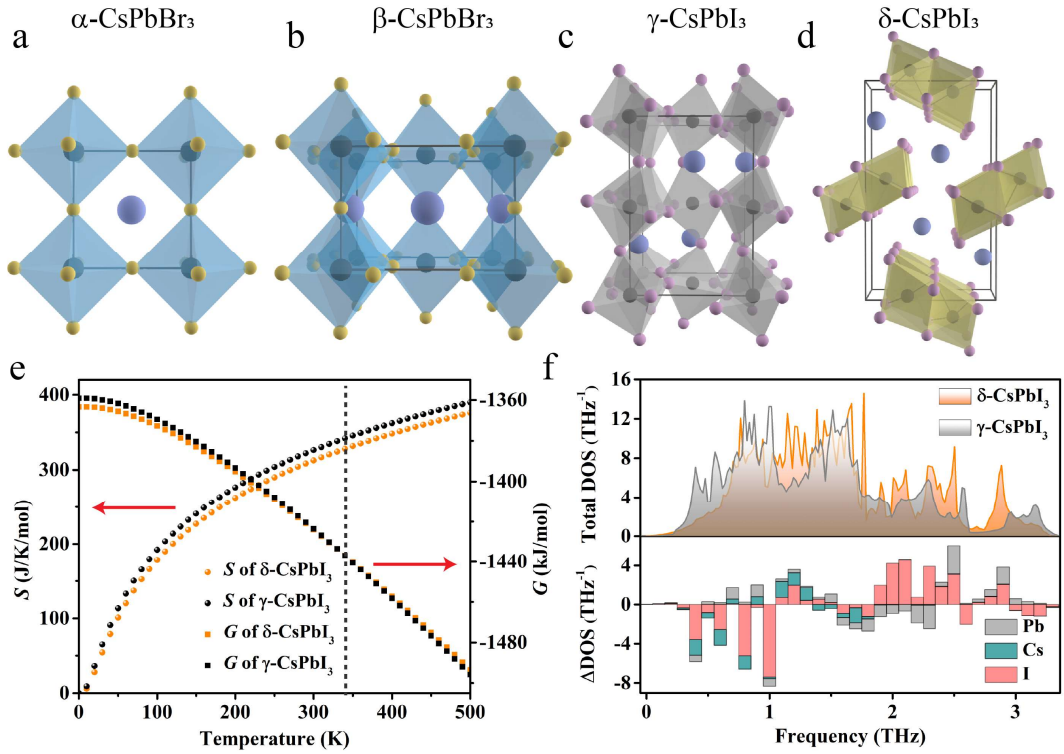
a
α-CsPbBr3
b
β-CsPbBr3
c
γ-CsPbI3
d
δ-CsPbI3
e
S (J/K/mol)
G (kJ/mol)
Temperature (K)
S of δ-CsPbI3
S of γ-CsPbI3
G of δ-CsPbI3
G of γ-CsPbI3
f
Total DOS (THz-1)
ΔDOS (THz-1)
Frequency (THz)
δ-CsPbI3
γ-CsPbI3
Pb
Cs
I

Figure 1. Crystal structures of $CsPbX_3$ (X=Br, I) and lattice dynamics calculations of reconstructive phase transition. From (a) to (d): α-$CsPbBr_3$, β-$CsPbBr_3$, γ-$CsPbI_3$, δ-$CsPbI_3$. Therein, Cs, Pb, I and Br atoms are shown in blue, gray, violet, and yellow, respectively. (e) The vibrational entropy (S_{vib}) and Gibbs free energy (G) for γ-$CsPbI_3$ and δ-$CsPbI_3$ calculated from 0 to 500 K. Vertical dashed lines indicate that the phase transition will occurs at 340 K. (f) The upper and lower panels demonstrate the DOSs for γ-$CsPbI_3$ and δ-$CsPbI_3$, and the difference of DOS ($\Delta DOS = DOS\delta - DOS\gamma$) between the two phases. The negative values indicate the increase of vibrational entropy from δ- to γ-$CsPbI_3$.

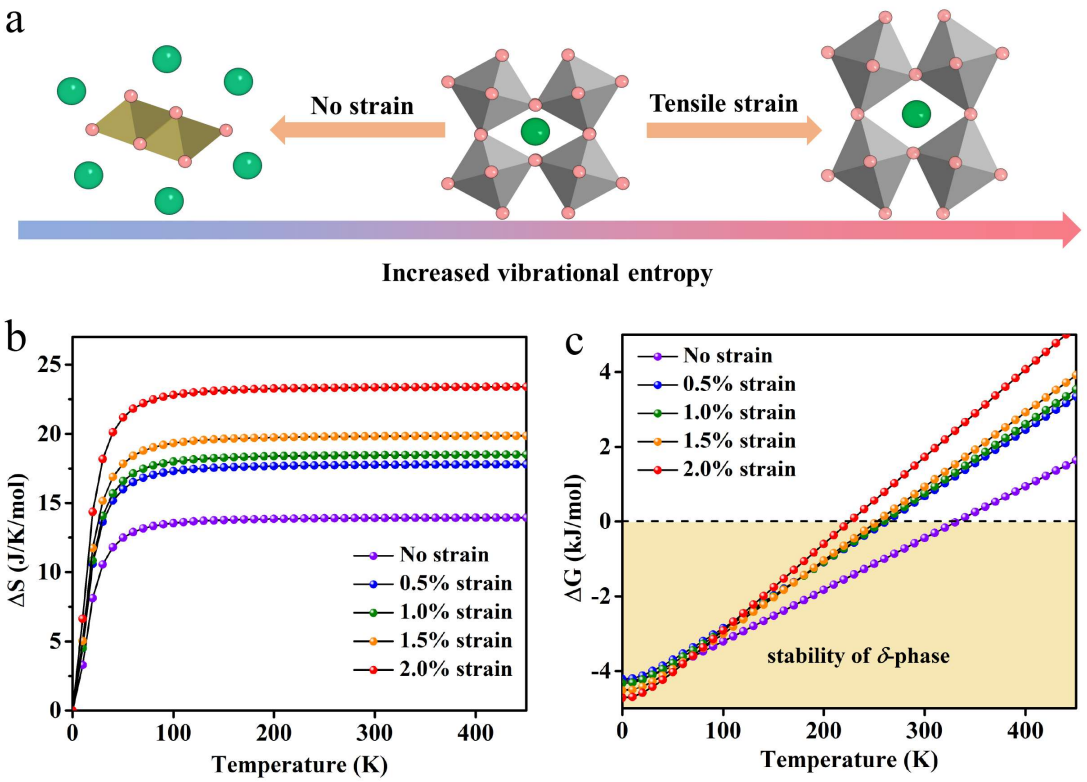

Figure 2. Strain engineering of γ-$CsPbI_3$. (a) Schematic illustration of strain engineering of γ-$CsPbI_3$. The difference of vibrational entropy ($\Delta S = S_\gamma - S_\delta$) (b) and free energy ($\Delta G = G_\delta - G_\gamma$) (c) per unit cell between γ- and δ-$CsPbI_3$ under different uniaxial strain conditions. The yellow area under the horizontal dashed line indicates that the δ-phase is stable in this range.

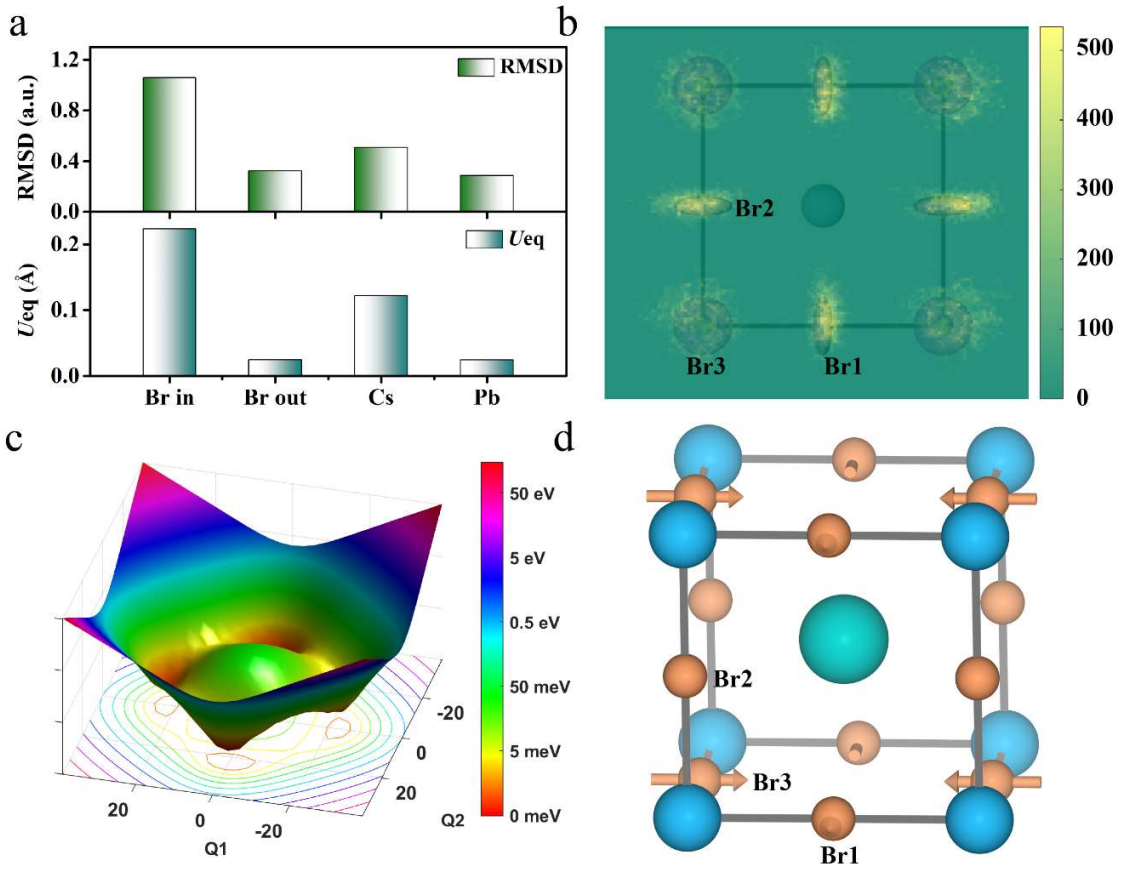

Figure 3. (a) Atomic root-mean-square displacements (RMSD) of Br, Cs and I of α-$CsPbBr_3$ from AIMD simulations (upper panel) and single-crystal X-ray diffraction experiments (lower panel). (b) The 2D PDFs of different Br atoms obtained by AIMD simulations and real crystal structure with anisotropic factor measured at 450 K projected normal to the (001) plane. (c) Contour plot of the energy varying Q1 and Q2 (amplitudes of M_3^+ and R_4^+ modes). (d) Displacement eigenvector corresponding to the soft phonon mode found at M point for α-$CsPbBr_3$, the irreducible representation is M_3^+. Color codes: Cs, cyan; Pb, blue; Br, orange.

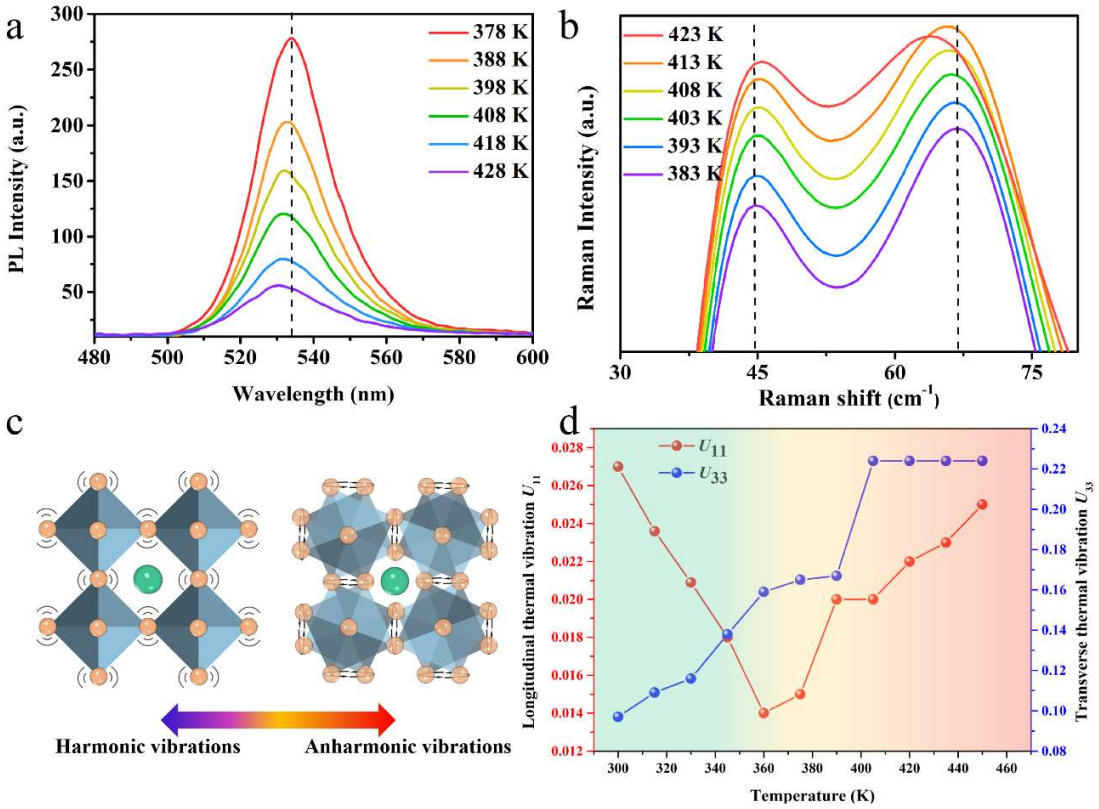

Figure 4. Experimental results of the disorder in α-$CsPbBr_3$. Variable-temperature photoluminescence (a) and Raman (b) of α-$CsPbBr_3$. (c) The schematic diagram of harmonic and anharmonic vibrations of cubic α-$CsPbBr_3$ perovskite. Different from the figure on the left, the disordered octahedral tilting on the right indicates a strongly anharmonic feature. (d) Temperature dependence of the thermal vibration of $CsPbBr_3$ in the range of 300-450 K.

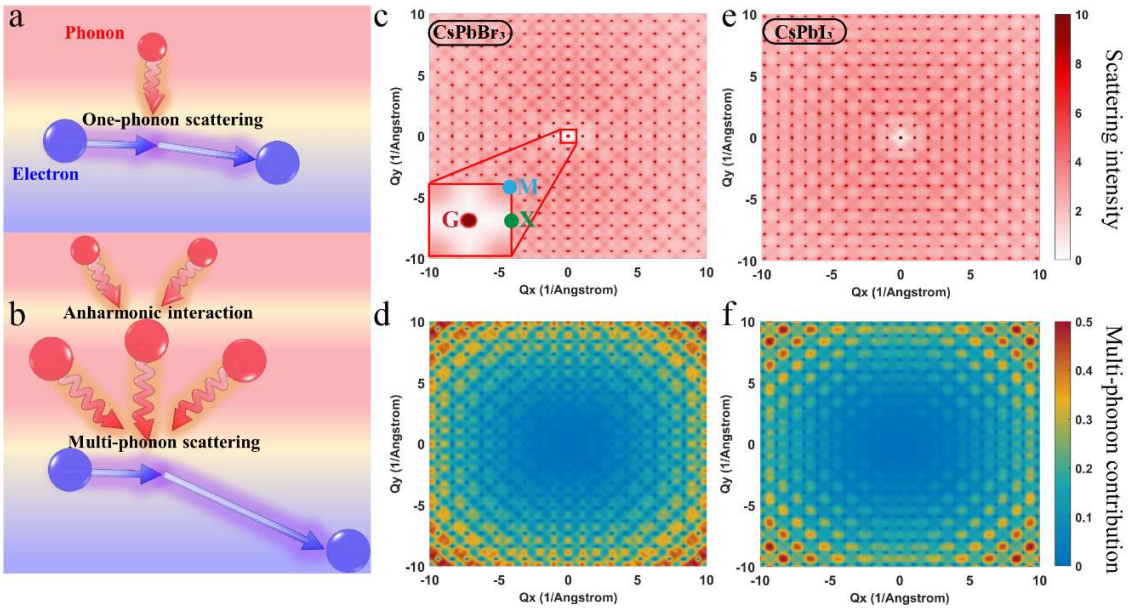

Figure 5. Phonon diffuse scattering of $CsPbX_3$. Schematic illustration of one-phonon scattering process (a) and multi-phonon scattering process under anharmonic interaction (b). (c) and (e) respectively represent the all-phonon scattering intensity of $CsPbBr_3$ and $CsPbI_3$, and the intensities were displayed with log10 scale to facilitate comparison. Percentage contribution of multi-phonon interactions to diffuse scattering of $CsPbBr_3$ (d) and $CsPbI_3$ (f) calculated as $P = I_{multi} / (I_1 + I_{multi})$ at different temperature, where I_1 and I_{multi} are one-phonon and multi-phonon scattering intensity.